

Sea Surface Temperature and Ocean Heat Content during Tropical Cyclones Pam (2015) and Winston (2016) in the Southwest Pacific Region

ASHNEEL CHANDRA^{a,b,c} AND SUSHIL KUMAR^c

^a *Geophysical Institute, University of Bergen, Bergen, Norway*

^b *Bjerknes Centre for Climate Research, Bergen, Norway*

^c *School of Information Technology, Engineering, Mathematics and Physics, The University of the South Pacific, Suva, Fiji*

(Manuscript received 31 January 2020, in final form 14 September 2020)

ABSTRACT: The sea surface temperature (SST) and upper-ocean heat content (OHC) have been explored along the track of two tropical cyclones (TCs): TC Pam (2015) and TC Winston (2016). These TCs severely affected the islands of Vanuatu and Fiji, in the South Pacific region (8°–30°S, 140°E–170°W). The SST decreased by as much as 5.4°C along the tracks of the TCs with most cooling occurring to the left of the TCs tracks relative to TC motion. SST cooling of 1°–5°C has generally been observed during both the forced and relaxation stages of TC passage. Argo profiles near the TCs revealed observable temperature-based mixed layer deepening. Subsurface warming was also observed post-TC passage from the temperature profile of one of the floats after the passage of both TCs. The OHC and heat fluxes are seen to play an important part in TC intensification as both these TCs intensified after passing over regions of high OHC and enhanced heat fluxes. Apart from the traditionally used OHC obtained up to the depth of the 26°C isotherm (Q_H), the OHC was also determined up to the depth of the 20°C isotherm ($Q_{H,20}$). The Q_H and $Q_{H,20}$ values decreased in the majority of cases post TC passage while $Q_{H,20}$ increased in one instance post-TC passage for both the TCs. $Q_{H,20}$ was also used to identify heat energy changes at deeper levels and it correlated well with the traditionally used OHC during the weaker stages of the TCs.

KEYWORDS: South Pacific Ocean; Vertical motion; Sea surface temperature; Thermocline; Oceanic mixed layer; Tropical cyclones

1. Introduction

Tropical cyclones (TCs) are severe terrestrial weather events that adversely affect coastal regions in most parts of the world. In particular, the small island states such as those of the South Pacific region are severely impacted by TCs. Global warming due to increased concentrations of greenhouse gases has been reported to lead to an increase in the frequency of intense TCs as well as an observable warming (positive trend) of the ocean (e.g., Emanuel 2005; Fyfe 2006; Pierce et al. 2006; Stowasser et al. 2007; Swart et al. 2018; Meyssignac et al. 2019; von Schuckmann et al. 2020). Chand and Walsh (2009, hereafter CW09), used 172 TCs, which occurred from 1970 to 2005 in the Fiji, Samoa, and Tonga region to study TC genesis and their subsequent tracks during different phases of El Niño–Southern Oscillation (ENSO). They found large regional variations in TC activity associated with ENSO phases in this region due to variations in the large-scale environmental conditions associated with ENSO phases. Chand and Walsh (2011) extended their work (CW09) to find any effect of the ENSO on TC intensity using TC data for the period 1985–2006 and reported that large-scale environmental factors affecting TC intensity were found to be favorable during La Niña periods and less favorable during El Niño periods, equatorward of 15°S. The opposite was true poleward of 15°S.

Gray (1968, 1988) studied global tropical cyclogenesis and reported several large-scale environmental conditions necessary for the formation of a TC. The four most widely agreed upon TC genesis conditions summarized by Bracken and Bosart (2000) include SSTs exceeding 26.5°C. Dare and McBride (2011a) reported that globally over the period 1981–2008, more than 93% and 98% of TCs occurred at SST values exceeding 26.5° and 25.5°C, respectively. The energy source for TCs is the ocean (Riehl 1950; Emanuel 1986) where energy is transferred between the air–sea interface in the form of the latent and sensible heat fluxes, which contribute to the cooling of the ocean surface. TCs lead to a reduction in the SST and mixed layer temperatures of the ocean via vertical mixing of the surface mixed layer water with colder water underneath (vertical entrainment) associated with strong TC winds resulting in wind stirring and vertical shear instability of wind-driven horizontal currents (e.g., Price et al. 1987; Jaimes and Shay, 2015).

The ocean responds to a TC in two stages called the “forced stage” when the TC is overhead and the “relaxation stage” following the TC passage of time scales typically of half a day and 5–10 days (Price et al. 1994), respectively. The forced stage is associated with enhanced mixed layer currents and substantial cooling of the sea surface and surface mixed layer due to vertical mixing and vertical advection in upwelling regimes created by wind stress (e.g., Price 1981, 1983; Price et al. 1994; Jaimes and Shay 2015). During the forced stage of a TC, vertical mixing and upwelling (or Ekman pumping) bring cooler thermocline water near the surface, which contributes to ocean surface cooling in the core of the storm whereas during the relaxation stage vertical shear instability of near-inertial horizontal currents is the dominant source of upper-ocean cooling

Supplemental information related to this paper is available at the Journals Online website: <https://doi.org/10.1175/MWR-D-20-0025.s1>.

Corresponding author: Sushil Kumar, kumar_su@usp.ac.fj

DOI: 10.1175/MWR-D-20-0025.1

© 2021 American Meteorological Society. For information regarding reuse of this content and general copyright information, consult the AMS Copyright Policy (www.ametsoc.org/PUBSReuseLicenses).

in the wake of the TC. Zhang et al. (2019) from the analysis of Quick Scatterometer Mission (QuikSCAT-R) wind field reported a good correlation (linear correlation coefficient of 0.51–0.59) between cold wake size and wind field size of TCs. Maximum SST cooling in the wake occurs within a week (relaxation stage) of TC passage with most tracks showing maximum SST cooling a day after the TC passage (Dare and McBride 2011b; Mei and Pasquero 2013). Most cooling due to TCs is observed to the left (right) of the track relative to the motion of the TC in the Southern (Northern) Hemisphere. This happens due to the effect of the translational velocity of the storm adding with the tangential velocity to the left (right) in the Southern (Northern) Hemisphere making the winds stronger on these sides of the storm, which contributes to more cooling of the sea surface (e.g., Price 1981; Mei and Pasquero 2013; Wang and Han 2014).

During TCs, sea surface warming due to dominant downwelling over warm, anticyclonic mesoscale oceanic features has also been observed and supported by numerical studies (Emanuel 1999; Jaimes and Shay 2009; Jaimes et al. 2011; Jaimes and Shay 2015). With the ocean playing a large part in the energy cycle of a TC, it has become an important area of research to study the interaction of TCs with the ocean. Several studies have been carried out on the oceanic energy available to TCs and TCs effect on near-surface and subsurface ocean layers (e.g., Shay et al. 1989; Korty et al. 2008; Jansen et al. 2010; Dare and McBride 2011a; Jullien et al. 2012; Toffoli et al. 2012; Lin et al. 2013; Ma et al. 2013; Guan et al. 2014; Jullien et al. 2014; Zhang et al. 2016; Yan et al. 2017). Apart from initial maximum wind speed, wind shear, latitude of the tropical cyclones, SST etc., a thermodynamic variable called upper-ocean heat content (OHC) also known as tropical cyclone heat potential (TCHP) is also considered important for the prediction of TC rapid intensification (Leipper and Volgenau 1972; Emanuel 1999; Lin et al. 2013). TCs often experience rapid intensification over warm mesoscale regimes (Jaimes and Shay 2015). Pun et al. (2013) using the sea surface height anomaly and SST dataset from 1993 to 2011 in the main development area of the western North Pacific Ocean found about a 10% increase in both the depth of the 26°C isotherm (typically represented by D26) and TCHP as compared to values in the 1990s. They also found an increase in the areas of high TCHP ($\geq 110 \text{ kJ cm}^{-2}$) and large D26 ($\geq 110 \text{ m}$) by 13% and 17%, respectively.

The southwest Pacific region is a comparatively less active region for TC development. While studies in the region have focused on intraseasonal to decadal trends of large-scale environmental features influencing TC genesis and tracks (Chand and Walsh 2010, 2011; Sharma et al. 2020), few studies have looked at TC–ocean interaction in the region. In this study, the SST and upper-ocean heat content have been determined along the tracks of TC Pam (9–15 March 2015) and TC Winston (6–26 February 2016), which severely affected the islands of Vanuatu and Fiji, respectively, causing widespread economic and infrastructure damage. We also determined the influence of oceanic heat content on the intensity of these two TCs and how these TCs influenced the near surface and subsurface layers of the ocean in terms of energy. TC Pam (March

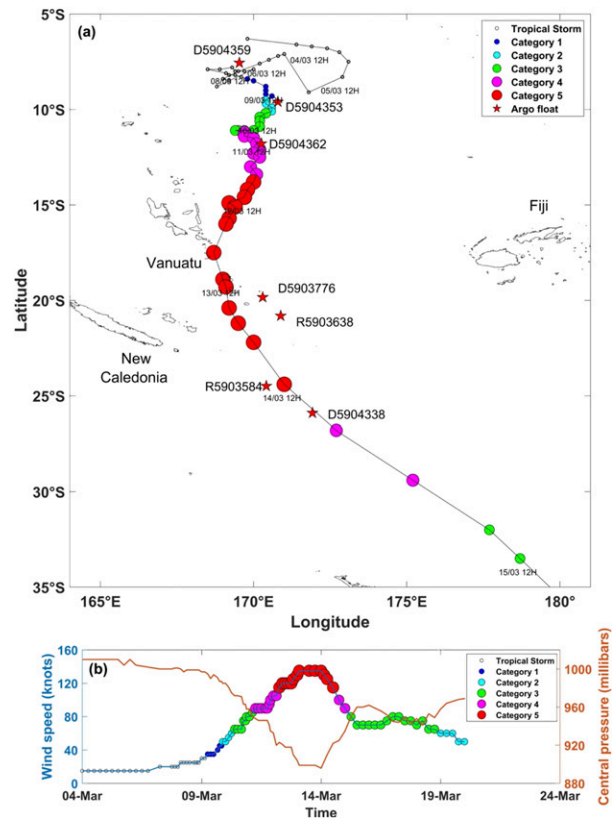


FIG. 1. (a) Track of TC Pam from 4 to 23 Mar 2015 with the location of seven Argo floats (red stars) along the track. (b) Maximum sustained winds (blue) and minimum central pressure (orange) for TC Pam.

2015) and TC Winston (February 2016) have been selected here as they were intense TCs (>category 3) and underwent rapid intensification just prior to making landfall.

2. Brief description of TCs studied

The TCs analyzed here caused significant damage to infrastructure as they made landfall over the nations of Vanuatu (TC Pam, March 2015) and Fiji (TC Winston, February 2016). The sudden change in intensity of these TCs has generated more interest in the region on the intensity forecasts of TCs making landfall.

a. TC Pam: March 2015

Figure 1a shows the track of TC Pam during 4–23 March 2015 with locations of seven Argo floats along the track. The variation of maximum sustained winds (blue) and minimum central pressure (orange) are shown in Fig. 1b. TC Pam was classified as a category-1 TC on 9 March 2015 when it was located at 8.5°S, 169.8°E near the Solomon Islands. With maximum sustained winds of 45 kt ($1 \text{ kt} = 0.514 \text{ m s}^{-1} = 1.852 \text{ km h}^{-1}$), it moved southeast at 3 kt (5.6 km h^{-1}). As TC Pam approached Vanuatu on 10 March following its southward trajectory, it intensified reaching category-3 strength with wind

speeds reaching 80 kt and central pressure of 963 mbar. On 11 March, Pam achieved wind speeds averaging 105 kt and was located at 11.2°S, 169.7°E, moving south-southwest at 2 kt. By 12 March, TC Pam had attained category-5 strength with a central pressure of 896 mbar and hurricane force winds of 135 kt extending 55.6 km from the eye. By this point, TC Pam was over 629.7 km in diameter. TC Pam moved in a south-southwest trajectory at 8 kt (14.8 km h^{-1}) during this time. The Joint Typhoon Warning Center (JTWC) reported that the TC generated high swells with heights reaching 12.1 m. On 13 March, TC Pam was located to the east of Port Vila, Vanuatu (18.3°S, 168.9°E) with an eye 27.7 km in diameter and was moving south-southwest at 8 kt (Gutro 2015). The Vanuatu Meteorological Services reported hurricane force winds of 255 km h^{-1} affecting the provinces of Shefa, Malampa, and Penama. By 15 March, TC Pam moved away from Vanuatu on a south-southeast path and began extratropical transition. TC Pam was classified as a category-5 cyclone according to the Australian Bureau of Meteorology.

b. TC Winston: February 2016

TC Winston had its origin as system 97P, which was upgraded to tropical storm TS 11P on 10 February 2016. The track of TC Winston from 5 February to 3 March 2016 with the locations of nine Argo floats along the track is shown in Fig. 2a. Figure 2b shows the variation of maximum sustained winds (blue) and minimum central pressure (orange) from 5 February to 3 March 2016. By 12 February, TS 11P became a category-3 TC with a wind speed of about 65 kt, centered at 17.7°S, 171.5°E and moved on a south-southeast trajectory at 6 kt (11.1 km h^{-1}). On 17 February, TC Winston was located at 17.9°S, 173°W with maximum sustained winds reaching 90 kt and with a central pressure of approximately 953 mbar and hurricane force winds extending 55.6 km. Winston had a diameter of 444.4 km and moved slowly east at 2 kt (Gutro 2017).

On 18 February, TC Winston recurved and began moving westward at 7 kt with winds averaging 100 kt. At this point, TC Winston generated waves with height of up to 8.5 m. It continued to intensify while moving toward Fiji and by 19 February, it was located at 17.3°S, 173.5°W with winds of 115 kt. On 20 February, TC Winston made landfall as a category-5 TC, on eastern Viti Levu, Fiji, with a maximum sustained wind of 150 kt and a minimum central pressure of about 884 mbar with gusts of 190 kt. On 21 February, TC Winston was located at 17.6°S, 174°E, moving west-southwest with maximum sustained winds of 110 kt. TC Winston began moving southward on 22 February and from 24 February encountered an area of strong vertical wind shear causing its winds to weaken to 45 kt.

TC Winston was reported as one of the most severe and devastating TCs in the Southern Hemisphere (Yulsman 2016). An intense stationary surface area of high pressure to the far south of Tonga prevented TC Winston from moving eastward and resulted in the TC recurving and heading toward Fiji. TC Winston made landfall to the northeast of Viti Levu, Fiji, on 20 February leaving a trail of destruction. TC Winston had attained maximum sustained winds of 233 km h^{-1} and gusts reaching 306 km h^{-1} . TC Winston affected close to 540 400 people ($\approx 62\%$ of the population) prompting the Fijian

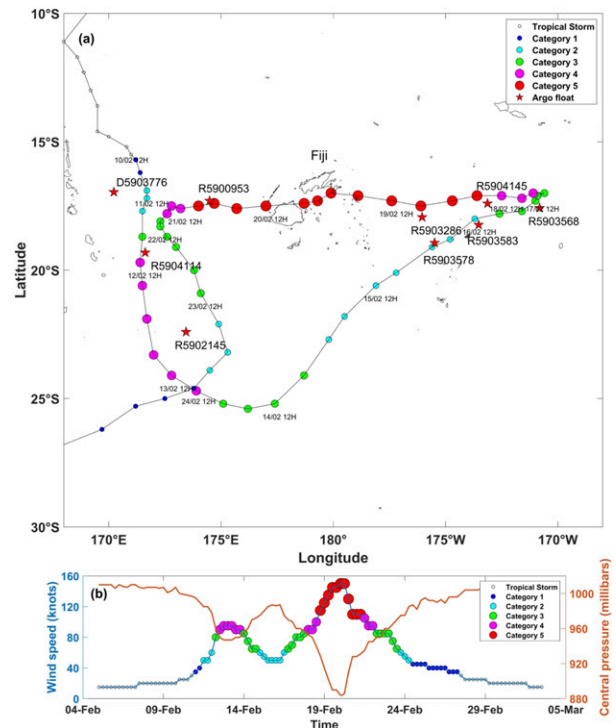


FIG. 2. (a) Track of TC Winston from 5 Feb to 3 Mar 2016 with the location of nine Argo floats (red stars). (b) Maximum sustained winds (blue) and minimum central pressure (orange) for TC Winston.

Government to declare a State of Natural Disaster, which extended to April 2016. The Lau and Lomaiviti groups, Taveuni, Tailevu, Naitasiri, and Ra provinces took most of the brunt with damages amounting close to \$900 million (U.S. dollars). For further details the reader is referred to Tropical Cyclone Winston, February 20, 2016 Post Disaster Needs Assessment Report, available online from the Global Facility for Disaster Reduction and Recovery (GFDRR) website (<https://www.gfdrr.org/en>).

3. Data and methodology

a. Data sources

TC best track data were retrieved from the Southwest Pacific Enhanced Archive for Tropical Cyclones (SPEARTC) of the Asia-Pacific Data-Research Center (<http://apdrc.soest.hawaii.edu/projects/spartc/>). This dataset consists of TCs in the southwest Pacific region (5° – 25° S, 135° E– 120° W) from the year 1840 onward and is constructed as described by Knapp et al. (2010). SPEArTC archives data for each TC at 6-h intervals showing the time, position, maximum sustained wind speed, central pressure at that point, maximum wind speed over the entire life of the TC, and number of points in the TC tracks.

SST data were obtained from the Group for High Resolution Sea Surface Temperature (GHRST) Level 4 Multiscale Ultrahigh Resolution (MUR) Global Foundation Sea Surface Temperature Analysis (v4.1). This dataset is hosted

by the JPL Physical Oceanography DAAC and can be accessed from the website: <https://podaac.jpl.nasa.gov/dataset/MUR-JPL-L4-GLOB-v4.1>. This dataset has been used for this study as it has high resolution of 0.01° global daily gridded data and incorporates microwave sensors needed to resolve SST variability in the presence of clouds. The GHRSSST dataset used in this study has been constructed from nighttime GHRSSST L2P skin and subskin SST observations from several instruments including the Advanced Microwave Scanning Radiometer-EOS (AMSR-E), the Advanced Microwave Scanning Radiometer 2, the Moderate Resolution Imaging Spectroradiometers (MODIS), the microwave WindSat radiometer, the Advanced Very High Resolution Radiometer (AVHRR), and in situ SST observations from the NOAA iQuam project. Further details and limitations about this dataset are given in research papers by [Chin et al. \(2017\)](#) and [Rudzin et al. \(2019\)](#). For this study, the SST data for the years 2015 and 2016 have been used.

Argo float data used in this study were obtained from the USGODAE Argo Page: http://www.usgodae.org/cgi-bin/argo_select.pl. The Argo project is an international collaboration of a global array of ≈ 3900 active profiling floats (as of May 2020) collecting temperature and salinity profiles from the upper ≈ 2 km of the ocean. These Argo floats usually have a 10-day cycle with some cycles as short as 1 day.

Latent and sensible heat flux data were obtained from NOAA Climate Data Record (CDR) of Ocean Heat Fluxes, version 2, that is available from the year 1988 at 3-hourly temporal and $1/4^\circ$ spatial resolutions over the global ice-free regions of the ocean. These data are available at the following website: <https://www.ncdc.noaa.gov/cdr/atmospheric/ocean-heat-fluxes>. One limitation of this dataset is that it sets an upper limit to the wind speed at 45 m s^{-1} due to unverifiable values outside of the training data range of the neural network used to obtain the heat fluxes ([Clayton et al. 2016](#)). As a result, this dataset is not very useful in regions near a TC that can have wind speeds exceeding this value of 45 m s^{-1} . However, the dataset is used to augment this study and gain some qualitative understanding of the influence of heat fluxes on TC intensity.

b. Data analysis

The analysis of SST variation and OHC changes was carried out for both the TCs. SST variability along the track of both the TCs was explored using the GHRSSST Level 4 MUR Global Foundation Sea Surface Temperature Analysis (v4.1) dataset. To find the variability in SST, the standard deviation of SST and the difference in SST along the track of the TCs were computed. For TC Pam these dates are 4–23 March 2015 and for TC Winston, the dates are 10–26 February 2016. To obtain the temperature with depth, a method similar to that suggested by [Nagamani et al. \(2012\)](#) was used where only Argo floats within a 2° radius from the TC track were selected, as this is usually the region most affected by the TC winds. The floats were classified as in the central region of the TC if the average distance of the pre- and post-TC float profiles were within 60 km of the nearest TC best track. If the average distance of the pre- and post-TC float profiles was further than 60 km but within 500 km of the nearest TC best track, the floats were classified as either in the left or right region of the TC relative to TC motion.

An important quantity to measure heat energy available to a TC is the tropical cyclone heat potential (TCHP), which is now more commonly known as upper-ocean heat content (OHC). [Leipper and Volgenau \(1972\)](#) initially explored the oceanic heat energy available to TCs and first defined the term “hurricane heat potential” or TCHP, that latter became known as OHC ([Shay et al. 2000](#)). Both are denoted by Q_H and represent the depth-integrated temperature anomaly from the surface to the depth of the 26°C isotherm. The OHC is an anomaly and is computed with a reference value of 26°C subtracted from each temperature observation at each depth. The Q_H according to [Leipper and Volgenau \(1972\)](#) is given as

$$Q_H(x, y, t) = \rho c_p \int_{z(T=26)}^0 [T(x, y, z, t) - 26] dz, \quad (1)$$

where c_p is the specific heat capacity of water at constant pressure ($4178 \text{ J kg}^{-1} \text{ K}^{-1}$), ρ is the average density of the upper ocean (1026 kg m^{-3}), and $T(x, y, z, t)$ is the temperature profile over the depth interval dz .

However, this definition was not useful to quantify the variability in ocean heat energy when the TC passed over regions where the SST was less than 26°C as well as post-TC passage. Hence, a lower temperature threshold of 20°C , which is usually representative of the thermocline, was used to calculate the heat energy contained in oceanic regions with SST up to 20°C . We define $Q_{H,20}$ (different from Q_H and TCHP, as it is with reference to the 20°C isotherm) as follows:

$$Q_{H,20}(x, y, t) = \rho c_p \int_{z(T=20)}^0 [T(x, y, z, t) - 20] dz. \quad (2)$$

For each Argo float, there were 12 profiles on average for the 4 months under investigation (2 months prior, during the month of, and 1 month after the passage of the TC). It was assumed that the Argo floats remained at a relatively fixed location in time when taking measurements on its ascent so that latitude and longitude remained constant. As the temperature is a function of latitude, longitude, depth and time, the above assumption simplifies temperature to a function of depth, $T(z)$. The assumption is valid as the Argo floats do not move considerably during a profile measurement, and the time interval between each measurement during a profile is negligible. This greatly simplified the integral:

$$\int_{z(T=T_0)}^0 [T(x, y, z, t) - T_0] dz$$

to

$$\int_{z(T=T_0)}^0 [T(z) - T_0] dz,$$

where T_0 is the reference temperature (20°C for $Q_{H,20}$ and 26°C for Q_H).

The integral was evaluated numerically using the trapezoid approximation. The depth of the 26° and 20°C isotherms, $z(T = 26^\circ\text{C})$ and $z(T = 20^\circ\text{C})$, respectively, were estimated by using linear interpolation of the temperature profile data.

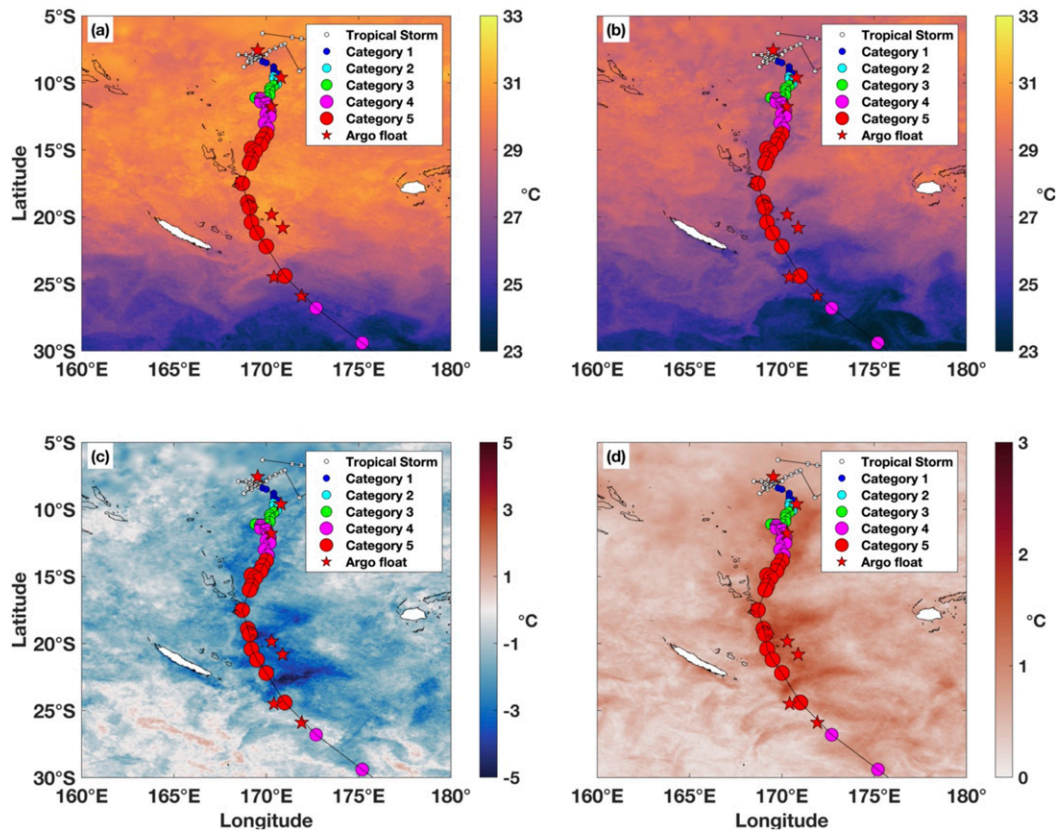


FIG. 3. Contour maps of (a) SST on 4 Mar 2015, (b) SST on 23 Mar 2015, (c) SST difference between 23 and 4 Mar 2015, and (d) SST standard deviation between 4 and 23 Mar 2015. Track of TC Pam is superimposed showing the intensity at each location with Argo floats shown as red stars.

As the temperature measurement at the surface ($z = 0$) was not available from Argo floats, the measurement nearest the surface was repeated, provided it was less than 5 m below the surface, similar to the method used by Nagamani et al. (2012). This depth range is usually within the mixed and isothermal layer where temperature is mostly uniform. Otherwise, $T(z = 0)$ was obtained from linear interpolation of the two temperatures in the profile immediately below the surface. This was necessary, as the integral requires temperature at the sea surface and the depth of the 26°C isotherm.

The near-surface heat content change (ΔH_A) and subsurface heat content change (ΔH_B) from Argo profiles immediately before and after the passage of a TC can be calculated using the following expressions from Park et al. (2011):

$$\Delta H_A = c_p \rho_0 \int_{z_c}^0 [T_2(z) - T_1(z)] dz, \tag{3}$$

$$\Delta H_B = c_p \rho_0 \int_{-400}^{z_c} [T_2(z) - T_1(z)] dz, \tag{4}$$

where c_p is the specific heat capacity of water at constant pressure ($4178 \text{ J kg}^{-1} \text{ K}^{-1}$), ρ_0 is the average density of the upper ocean (1026 kg m^{-3}), $T_1(z)$ is the temperature profile before the TC passage, $T_2(z)$ is the temperature profile after

the TC passage, and z_c is the depth at which the pre-TC, $T_1(z)$ and post-TC, $T_2(z)$ profiles intersect.

The values of ΔH_A and ΔH_B using Eqs. (3) and (4), respectively, were computed where possible using pre- and post-TC passage Argo profile data.

4. Results

a. TC Pam

For TC Pam, 50 Argo floats were identified in the region bounded by latitudes 5°–35°S and longitudes 165°E–175°W from January to April 2015. Only seven Argo floats met the data analysis criteria (Nagamani et al. 2012) and the profiles for these seven floats were examined up to 2 months prior, during the month of, and 1 month after the passage of the TC to sufficiently understand the pre- to post-TC profiles. These floats were also selected on the basis that within the 4 months under investigation, the floats did not move greater than 2° from the location that the floats were at immediately before the TC. The SST variation along the track of this TC is shown in Fig. 3. A contour plot of SST on 4 March 2015 shows that the SST was greater than 30°C in the region (0.5°–1°C above the 1971–2000 climatology, see Fig. S1 in the online supplemental material) when it was a tropical storm (Fig. 3a). Following the passage of

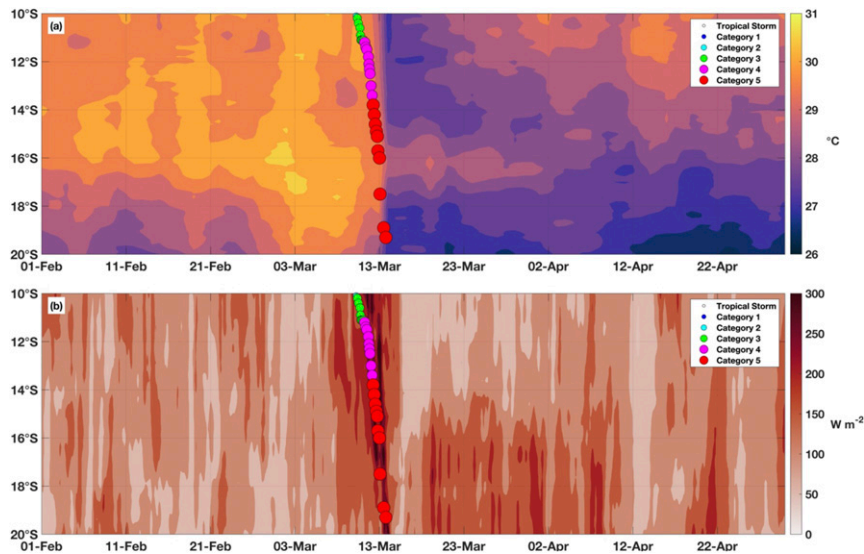


FIG. 4. Hovmöller plots of (a) SST and (b) latent plus sensible heat flux averaged between 168° and 172°E longitudes from 1 Feb to 30 Apr 2015. The track of TC Pam is superimposed.

TC Pam on 23 March, a reduction in SST along the track is evident as shown in Fig. 3b. The difference in SST between 23 and 4 March 2015 shows a reduction (mainly associated with the relaxation stage) by 1°–3°C along the track as seen from Fig. 3c. The maximum reduction of 5.4°C in the SST along the track was in the area covering 16°–24°S, 170°–175°E where the TC was overhead during 13–14 March 2015. The largest SST cooling is also observed to occur to the left of the track relative to TC motion. The largest variability in SST during the 20 days is observed to be near the track of TC Pam as shown in Fig. 3d.

Figure 4a presents a Hovmöller plot of daily SST averaged between longitudes 168°–172°E from 1 February to 30 April 2015. The SST Hovmöller plot reveals SST changes during the different intensities of TC Pam. SST reductions of 2°–4°C within 4 days during categories 3 and 4, and 1°–2°C within a day (with more persistent cooling of 2°–3°C extending over a month) during the category-5 stage were observed along the track of TC Pam as seen in Fig. 4a. SST cooling of up to 2°C was associated with the forced stage of TC Pam mostly during the category-5 stage while cooling of up to 4°C was associated with the relaxation stage of the TC. This finding is consistent with the findings of previous studies (e.g., Prasad et al. 2009; Mei and Pasquero 2013) who found SST reductions of about 3°C with most cooling occurring about a week after TC passage (relaxation stage). Less noticeable cooling during part of the category-5 stage of TC Pam could be due to the TC having a larger translational velocity during the intense stage as seen from the increased distance between consecutive points in Fig. 4a, which has also been reported by Mei and Pasquero (2013). SST cooling is also seen to be more persistent during the intense stage of the TC. This may be a result of the cooling occurring at higher latitudes in addition to the TC occurring toward the end of the summer season, which has been reported to result in the sea surface not being able to recover from the cooling (Dare and McBride 2011b). Latent plus Sensible Heat

Fluxes as shown in Fig. 4b are also enhanced along the track of TC Pam, providing some qualitative information on the air–sea energy transfer occurring to provide “fuel” for the TC. The enhanced heat fluxes along the track of the TC can also explain the intensification of TC Pam resulting in the TC attaining category-5 strength.

To find the subsurface effects of the TC, Argo floats along the track of the TC were identified. The average temperature profiles in the left, central, and right regions of TC Pam are shown in Figs. 5a–c for ocean depth of up to 400 m. The horizontal bars indicate one standard deviation in the temperature from the mean value at each depth. To get the averaged profile in the left region shown in Fig. 5a of TC Pam, three pre- and post-TC profiles from floats D5903776, D5904353, and R5903638 were used. The central region of TC Pam had three floats (D5904338, D5904362, and R5903584), which were used to create the average profiles in the central region (Fig. 5b). There was only one float (D5904359) located to the right of TC Pam, which is shown in Fig. 5c. Argo profiles show significant surface temperature changes, consistent with SST reductions in all the three regions of the TC. The central and right post-TC profiles show large cooling extending up to 360 m depth while the left region of the TC shows noticeable cooling only up to 60 m depth. The profile in the left region also shows more deepening of the mixed layer while not much deepening is seen in the profiles located in the central and right regions of the TC.

The variability in ocean heat content, Q_H and $Q_{H,20}$ 2 months prior, during, and 1 month after the passage of TC Pam averaged in the left, central, and right region to the TC track is shown in Figs. 6a and 6b. The Q_H is found to decrease in six of the seven Argo floats (Fig. S2a). The Q_H value post TC passage for float D5904338 is not defined as the SST was below the 26°C threshold. The $Q_{H,20}$ values shown in Fig. 6b are similar to Q_H values and both show a decrease in the OHC following the passage of the TC. More evident reductions in Q_H are seen in

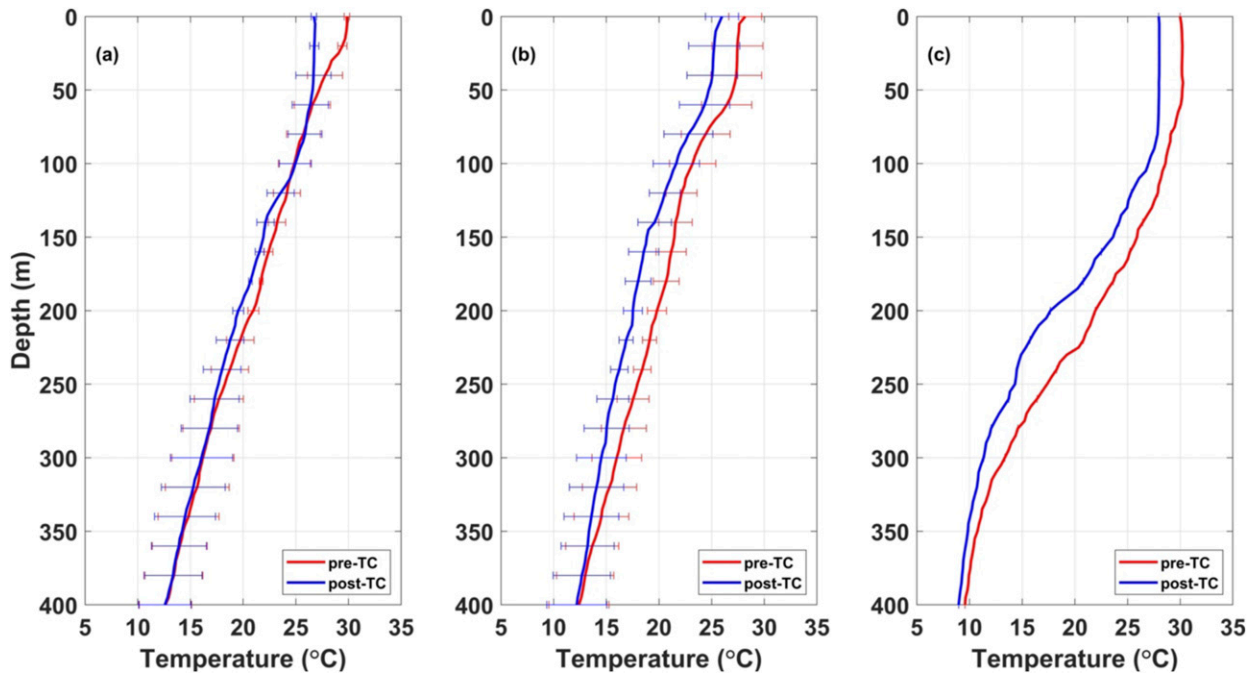


FIG. 5. Averaged Argo temperature profiles to the (a) left, (b) center, and (c) right of the track of TC Pam. Profiles in red (blue) are before (after) TC passage. Error bars are one standard deviation from the mean profiles. The location of the profiles is relative to TC motion.

profiles D5904353 (located to the left), D5904359 (located to the right), and D5904362 (located near the center) (Fig. S2a). For float D5904359, the TC was still in the tropical storm stage while TC Pam was of categories 2 and 4 when passing floats D5904353 and D5904362, respectively. Table 1 summarizes the

changes in Q_H and $Q_{H,20}$ values pre- and post-TC Pam and the linear correlation coefficient (r) between Q_H and $Q_{H,20}$ values for six of the seven floats near the track of the TC Pam. Generally, Q_H and $Q_{H,20}$ values decreased post-TC passage. With the removal of the negative r for float R5903638, the

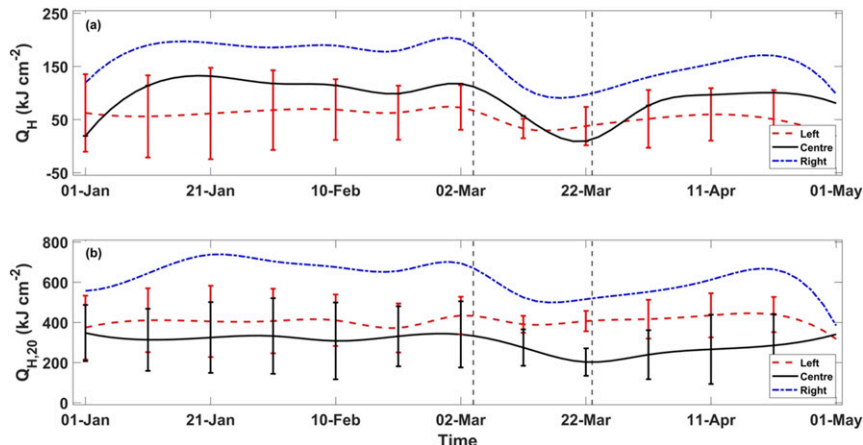


FIG. 6. Upper-ocean heat content illustrating (a) Q_H and (b) $Q_{H,20}$ values determined from the seven Argo floats within 2° radius of the track of TC Pam during the months of January–April 2015. The black curve is the averaged upper-ocean heat content in the central region (within 60 km) while the red (blue) curve is the averaged upper-ocean heat content in the left (right) region, i.e., between 60 and 500 km, of the TC. The location of the profiles is relative to TC motion. The black vertical dashed lines indicate the onset of TC Pam on 4 Mar 2015 and the dissipation/extratropical transition of TC Pam on 23 Mar 2015. Error bars are one standard deviation from the mean values.

TABLE 1. Values of Q_H and $Q_{H,20}$ pre- and post-TC Pam passage during the month of March 2015 and linear correlation coefficients (r) between Q_H and $Q_{H,20}$. The average distance of the float from the nearest TC best track as well as the distance moved by the float from the pre-TC profile is also listed.

Argo float	Pre-TC Q_H (kJ cm^{-2})	Post-TC Q_H (kJ cm^{-2})	Pre-TC $Q_{H,20}$ (kJ cm^{-2})	Post-TC $Q_{H,20}$ (kJ cm^{-2})	r	Avg distance from nearest TC best track (km)	Distance moved from pre-TC location (km)
D5903776	60.6	27.2	446.6	393.8	0.55	149.9	28.5
D5904338	0.9	—	187.6	157.0	—	52.6	40.5
D5904353	114.6	16.0	522.3	347.0	0.97	106.3	19.6
D5904359	192.1	82.9	677.2	476.5	0.95	80.7	29.7
D5904362	116.3	0.6	492.7	186.5	0.95	11.4	22.7
R5903584	24.9	0.6	317.6	262.8	0.47	27.3	41.4
R5903638	45.6	18.3	369.1	379.3	-0.14	173.1	16.6

mean r becomes 0.78 for the five floats. This translates to Q_H values being able to explain about 60% of the variance in $Q_{H,20}$ values and vice versa. Of the six floats analyzed, three (D5904353, D5904359, and D5904362) showed r greater than 0.90 (Table 1). This may indicate that $Q_{H,20}$, in some cases could be of use in monitoring the variability in ocean energy underneath TCs in regions with SST less than 26°C and as low as 20°C once it has formed. However, float R5903638 (located to the left of the TC relative to TC motion) shows an increase in $Q_{H,20}$ after the passage of TC Pam.

b. TC Winston

For TC Winston, 60 floats were identified in the region 10°–30°S, 170°E–170°W from December 2015 to March 2016, however, only eight Argo floats were within the 2° radius of TC Winston, while another float (R592145) was further than 2° but within 500 km of the TC track. This float is also included in our analysis for TC Winston. The profiles of these floats were analyzed up to two months prior, during the month and one month after the passage of this TC. The SST variation along the track of TC Winston before and after its passage is shown in Figs. 7a–d. Figure 7a shows SST above 30°C (1°–1.5°C above 1971–2000 climatology see Fig. S3) in most of the region while TC Winston was still a tropical depression on 10 February 2016. After the passage of TC Winston on 26 February 2016 (Fig. 7b), the SST decreased to about 25°–28°C in some regions near the track of TC Winston. This corresponds to a decrease in SST of 2°–5°C mainly associated with the relaxation stage of TC passage (Fig. 7c). The maximum reduction in SST of 5.4°C is observed in the region 17°–22°S, 171°–176°E, where TC Winston was weakening while slowly moving and slightly recurving from its westward trajectory after making landfall. This observation is also consistent with results reported by Mei and Pasquero (2013), who showed that slow moving TCs produce greater SST reductions. Most observable SST cooling occurred to the left of the TC track relative to TC motion (Figs. 7b,c) similar to the cooling pattern observed during TC Pam. Figure 7d shows large variability from the mean SST (1°–3°C) near the track of TC Winston with the largest variability coinciding with where the largest reduction in SST is observed.

Figures 8a and 8b shows the Hovmöller plot for SST and latent plus sensible heat flux averaged between latitudes 16°–19°S for the months of January to March 2016. Most SST cooling of 1°–5°C is seen during categories 3 and 4 of the TC

and mainly associated with the forced stage of the TC as SST cooling is observed to occur within a day. No observable SST cooling is seen in regions where the TC has a large translational velocity (between longitudes 176°–178°E) as seen in Fig. 8a. Note that the longitudinal band 176°E–180° has a large island, which may mask TC Winston's effect on SST near that region due to the TC making landfall. Latent plus sensible heat fluxes are seen to be enhanced about 3–5 days prior to TC Winston making landfall around 180° as seen in Fig. 8b. As mention before, the longitudinal band 176°E–180° has the island of Viti Levu, the largest island of Fiji and so the heat fluxes is somewhat contaminated by heat fluxes over land. It should also be noted that the heat flux data has limitations when wind speed exceeds 45 m s⁻¹.

Argo floats along the track of TC Winston were identified. The average temperature profiles in the left, central, and right regions of TC Winston are shown in Figs. 9a–c. To obtain the averaged profile in the left region (Fig. 9a) of TC Winston, two pre- and post-TC profiles from floats R5902145 and R5904145 were used. The central region of TC Winston had six floats (R5900953, R5904114, R5903286, R5903568, R5903578, and R5903583), which were used to create the averaged profile in the central region as shown in Fig. 9b. There was only one float (D5903776) located to the right of TC Winston, which is shown in Fig. 9c. As TC Winston followed a loop path, it passed near some floats more than once and in some instances the floats were in different regions of the TC. To identify the region of the TC a float was located, we used the region of the TC where a float was located at when the TC first approached the Argo float. The averaged Argo profiles to the left of TC Winston show observable deepening of the mixed layer as well as surface cooling extending up to 60 m depth. There is also some evidence of subsurface warming occurring in the 60–80 m depth range of the pre- and post-TC profiles as seen in Fig. 9a. However, this cannot be distinguished due to the uncertainty as a result of the profile averaging. The central region of the TC shows surface cooling in the upper 30 m, after which the pre- and post-TC profiles become virtually indistinguishable as seen in Fig. 9b. The profile to the right of the TC shows the pre- and post-TC temperature conditions to be almost identical. This could be due to only one float being present in this region. As a result, we cannot infer the averaged pre- and post-TC temperature conditions to the right of TC Winston due to limited temperature profiling in this region.

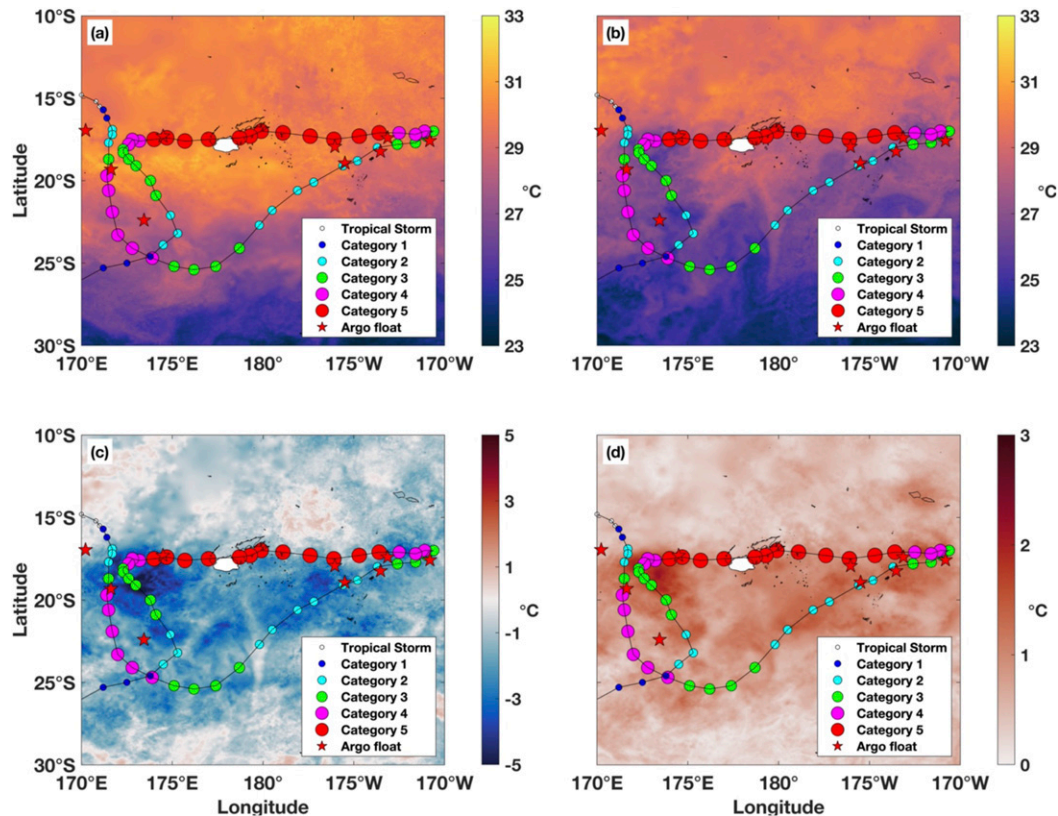


FIG. 7. Contour maps of (a) SST on 10 Feb 2016, (b) SST on 26 Feb 2016, (c) SST difference between 26 and 10 Feb 2016, and (d) SST standard deviation between 10 and 26 Feb 2016. Track of TC Winston is superimposed showing the intensity at each location with Argo floats shown as red stars.

Figures 10a and 10b show the variations in Q_H and $Q_{H,20}$ for the floats in the left, central and right region of the track of TC Winston. Unlike for TC Pam, there is more variability in both $Q_{H,20}$ and Q_H during TC Winston (see Fig. S5). Table 2 summarizes Q_H and $Q_{H,20}$ values pre- and post-TC Winston along with the r values between Q_H and $Q_{H,20}$. The removal of the two negative correlation coefficients gives a mean value of $r = 0.47$ for the seven floats. This shows that Q_H can explain the variance in $Q_{H,20}$ values for about 22% of the time. Seven of the nine Argo floats (R5900953, R5904114, R5903286, R5903568, R5903578, R5903583, and R5904145) show reductions in Q_H values while seven floats (R5900953, R5902145, R5903286, R5903568, R5903578, R5903583, and R5904145) also show reductions in $Q_{H,20}$ values post TC passage (see Fig. S5). Unlike the case for Pam, the r values between Q_H and $Q_{H,20}$ is lower for TC Winston as compared to TC Pam ($r = 0.78$ for TC Pam and $r = 0.47$ for TC Winston).

5. Discussion

SST variability was analyzed along the tracks of two TCs in the South Pacific Region that occurred during the year 2015 (TC Pam) and 2016 (TC Winston). Both these TCs with maximum translation speeds of 4.1 m s^{-1} (or 8 kt, TC Pam) and 3.1 m s^{-1} (or 6 kt, TC Winston) were slow moving TCs. Price

(1981) classified hurricanes with translation speed of about 3 and $\geq 6 \text{ m s}^{-1}$ as slow and rapidly moving, respectively. Price (1981) summarized earlier studies on changes in SST due to slow and rapidly moving hurricanes and reported a decrease in SST from 2° to 6°C due to slow moving hurricanes and 1° to 3°C due to rapidly moving hurricanes. The SST changes along the tracks during the relaxation stage of the two TCs of interest in this study decreased by about 2° – 4°C as seen from the SST Hovmöller plots for both TCs (Figs. 4, 8). While during TC Pam, SST cooling was associated with both the forced and the relaxation stage of TC passage, during TC Winston, most of the observed SST cooling was associated with the forced stage of TC passage. The magnitude of SST decrease is consistent with previous studies (Price 1981; Emanuel 1999; Zedler et al. 2002; Cione and Uhlhorn 2003; Prasad et al. 2009; Sanford et al. 2011; Guan et al. 2014) that have reported on hurricanes cooling the sea surface by 1° – 6°C depending upon their translational speed.

Strong vertical mixing of the warm water in the upper ocean with colder thermocline water during TCs can lead to a reduction in the SST associated with the forced stage of TC passage (Korty et al. 2008). Following the passage of a TC i.e., during the relaxation stage (wind stress is nearly zero), the ocean adjusts toward equilibrium through a geostrophic adjustment process generating strong near-inertial internal currents. The rotation of these currents at near inertial frequencies

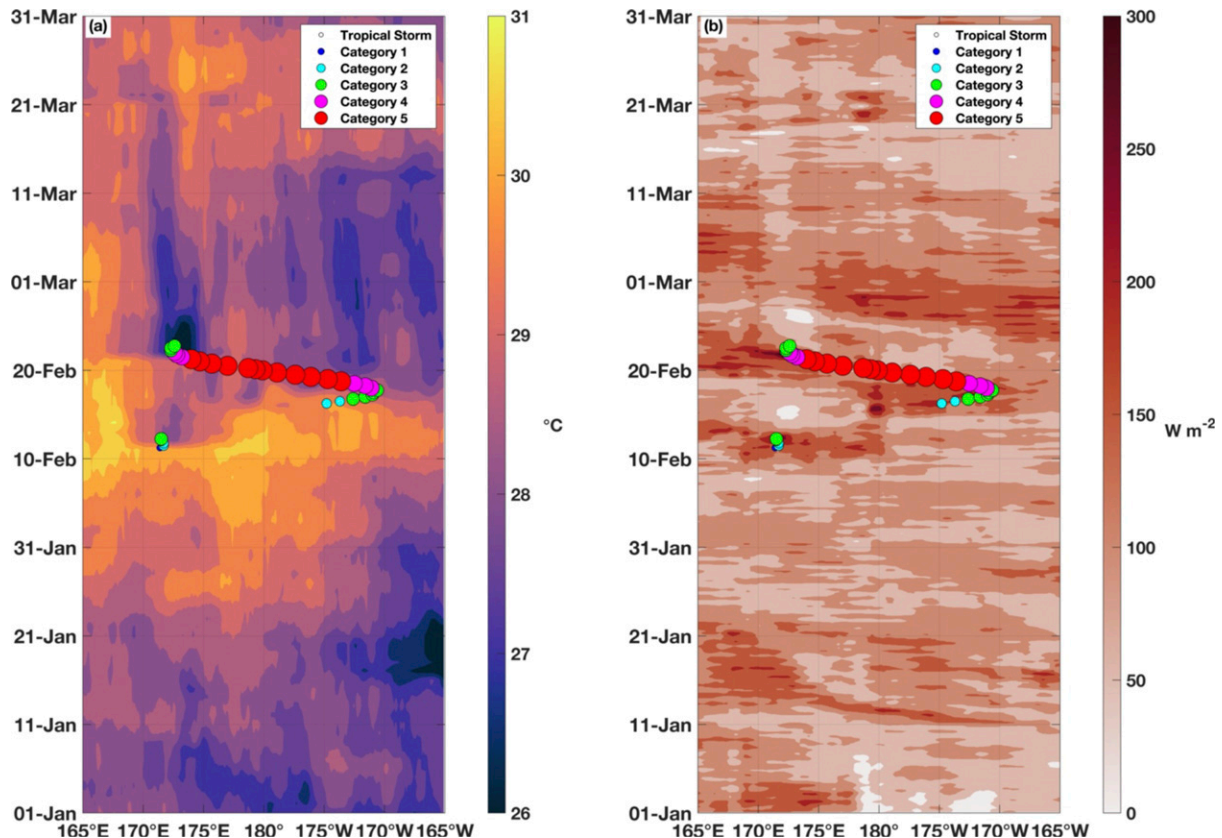


FIG. 8. Hovmöller plots of (a) SST and (b) latent plus sensible heat flux averaged between 16° and 19° S latitudes from 1 Jan to 31 Mar 2016. The track of TC Winston is superimposed.

drives near-inertial pumping and vertical shear instability, which are cooling mechanism in the wake of the TC (e.g., Price 1981, 1983; Gill 1984; Zhai et al. 2009; Jaimes et al. 2011; Rayson et al. 2015). The reduction in SST was also evident in Argo profiles post-TC passage. The deepening of the temperature-based mixed layer was evident from the Argo profiles mainly in the left region of both TCs, which is also where most cooling of SST is observed. This may be associated with turbulent mixing and upwelling occurring due to the wind stress from the TC.

Both TC Pam and TC Winston showed significantly more cooling toward the left of the track, which agrees with previous studies (e.g., Price 1981; Mei and Pasquero 2013). In the Southern Hemisphere, the left side of the TCs tracks generally have stronger winds due to the translational velocity of the TCs adding with the tangential velocity of the winds. More cooling was also found where the TCs had slower translational velocity, which allowed the TCs to spend a long time over these regions to cause greater cooling. Subsurface warming associated with both TCs was evident from one of the Argo profiles, which could possibly be attributed to the mixing of heat down the water column as suggested by Korty et al. (2008).

TCs interacting with eddies have also been observed to affect SST response to TCs. Cold core eddies are found to enhance SST reductions while warm core eddies inhibit large SST reductions post TC passage (Ma et al. 2017). However, the

effect of eddies on TCs has not been a part of this study and is suggested for future work. The presence of barrier layers in the ocean can act to reduce entrainment of cooler waters from deeper levels resulting in reduced SST cooling due to TCs as reported in a few studies (e.g., Wang et al. 2011; Balaguru et al. 2012; Yan et al. 2017). The presence of a barrier layer with a thickness of 5–15 m has been reported to reduce surface cooling by 0.4° – 0.8° C (Wang et al. 2011). SST restoration time to climatological values has been reported to occur within 5–30 days (e.g., Hart et al. 2007; Dare and McBride 2011b; Knaff et al. 2013) but restoration due to near-surface cooling could take longer than 30 days after the passage of a TC (Park et al. 2011).

The near-surface (from the sea surface to about 60 m) and subsurface (approximately between 60 and 400 m) characteristics of temperature and salinity are also affected by TCs (e.g., Elsberry et al. 1976; Emanuel 2001; Korty et al. 2008; Jansen et al. 2010; Park et al. 2011; Knaff et al. 2013; Guan et al. 2014; Wang and Han 2014). Our results show both near-surface and subsurface cooling for both the TCs with stronger cooling observed during TC Pam when compared to TC Winston and more evident toward the left and center of the track for both the TCs (Figs. 5, 9). The findings of Park et al. (2011) using Argo profiles showed that for intense TCs (categories 4 and 5), near-surface cooling and subsurface warming were largely due to vertical mixing, while the dominating factors during weaker TCs

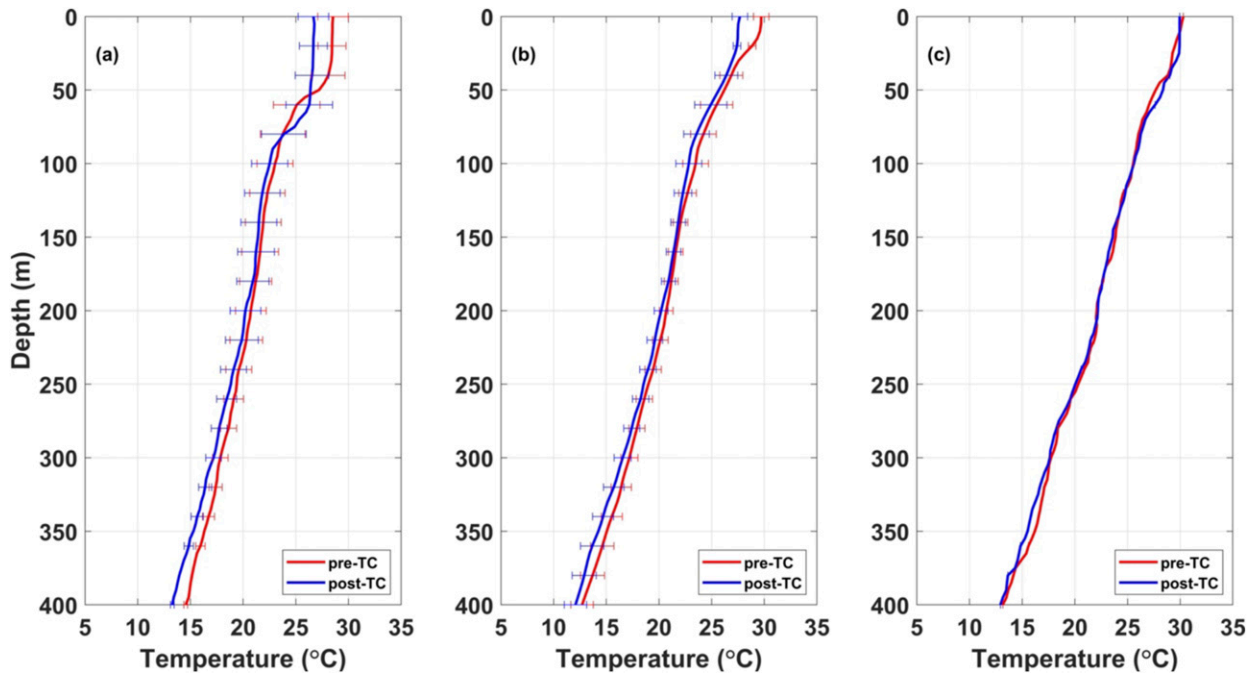


FIG. 9. Averaged Argo temperature profiles to the (a) left, (b) center, and (c) right of the track of TC Winston. Profiles in red (blue) are before (after) TC passage. Error bars are one standard deviation from the mean profiles. The location of the profiles is relative to TC motion.

were sensible and latent heat fluxes associated with upwelling with which our results are consistent. Wang and Han (2014) examined the responses of two consecutive TCs in the Bay of Bengal and found vertical mixing and upwelling responsible for near-surface cooling.

Variability in OHC (Q_H) was explored for both TC Pam and TC Winston with the aim of using these heat content changes to identify the TCs influence on the ocean subsurface. Q_H represents the ocean heat anomaly contained in waters warmer than 26°C. The traditionally used Q_H is defined up to the 26°C

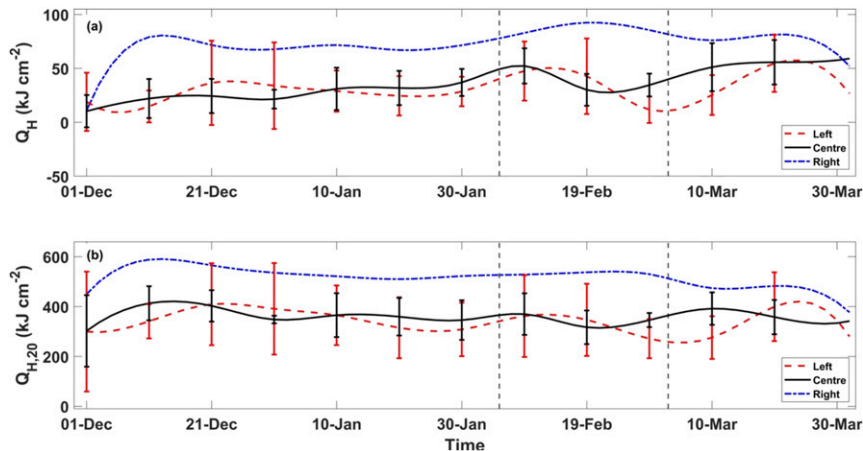


FIG. 10. Upper-ocean heat content illustrating (a) Q_H and (b) $Q_{H,20}$ values determined from nine Argo floats along the track of TC Winston during the months of December 2015–March 2016. The black curve is the averaged upper-ocean heat content in the central region, i.e., within 60 km, while the red (blue) curve is the averaged upper-ocean heat content in the left (right) region, i.e., between 60 and 500 km, of the TC. The location of the profiles is relative to TC motion. The black vertical dashed lines indicate the onset of TC Winston on 5 Feb 2016 and the dissipation/extratropical transition of TC Winston on 3 Mar 2016. Error bars are one standard deviation from the mean values.

TABLE 2. Values of Q_H and $Q_{H,20}$ pre- and post-TC Winston passage during the month of February 2016 and linear correlation coefficients (r) between Q_H and $Q_{H,20}$. The average distance of the float from the nearest TC best track as well as the distance moved by the float from the pre-TC profile is also listed.

Argo float	Pre-TC Q_H (kJ cm^{-2})	Post-TC Q_H (kJ cm^{-2})	Pre-TC $Q_{H,20}$ (kJ cm^{-2})	Post-TC $Q_{H,20}$ (kJ cm^{-2})	r	Avg distance from nearest TC best track (km)	Distance moved from pre-TC location (km)
D5903776	80.0	91.4	527.8	533.1	0.21	160.0	12.4
R5900953	32.8	10.8	266.6	195.7	0.75	39.4	32.6
R5902145	26.4	—	243.1	238.2	—	236.3	39.9
R5904114	43.3	22.4	334.6	348.4	-0.03	53.4	13.4
R5903286	65.2	39.7	396.1	358.6	0.71	31.3	36.7
R5903568	72.7	28.3	493.6	333.1	0.15	23.9	47.9
R5903578	59.1	25.5	365.5	292.2	0.03	32.0	23.4
R5903583	41.3	21.3	323.5	316.2	0.70	54.7	49.5
R5904145	78.6	43.2	474.0	370.6	0.76	66.6	36.2

isotherm and $Q_{H,20}$ defined similarly but up to the 20°C isotherms. These two quantities were estimated for both the TCs using Argo floats within mostly 2° of their tracks. This also highlights the limitations of the conventional definition of Q_H , which usually cannot be used to find the variability in oceanic energy over the regions with SSTs below 26°C. The Q_H and $Q_{H,20}$ values decreased in the majority of the post-TC passage cases. Shay et al. (2000) using airborne profilers deployed inside TCs showed that regions of high oceanic heat content could offset the cooling effect (negative feedback) of TCs on the ocean and cause TC intensification. Argo floats and expendable bathythermographs (XBTs) deployed by research ships provide valuable information about Q_H if these fall along or near the track of TCs. It is difficult to monitor Q_H uniformly due to the distribution of ocean profilers and so Q_H is usually estimated from satellite altimetry using sea surface height anomalies (e.g., Goni et al. 2009; Nagamani et al. 2012). Recently, significant improvements to satellite-based estimates of Q_H have been achieved by considering climatology from hundreds of thousands of in situ measurements of temperature (e.g., Meyers et al. 2014; McCaskill et al. 2016).

TCs extract energy from the ocean in the form of latent and sensible heat fluxes, which contributes to the observed reduction in SST and OHC after the passage of TCs (e.g., Toffoli et al. 2012; Wang and Han 2014). However, $Q_{H,20}$ increased in one instance post-TC passage during both the TCs. During TC Pam, float R5903638 (located to the left) showed an increase in $Q_{H,20}$ of 10.1 kJ cm^{-2} post TC passage. This float moved a distance of 17 km post-TC passage. The temperature profiles of float R5903638 (not shown) revealed signatures of near surface cooling and subsurface warming as described by Park et al. (2011). The near-surface heat content change (ΔH_A) and subsurface heat content change (ΔH_B) were estimated to be -32.1 and 49.3 kJ cm^{-2} , respectively.

For the calculation of Q_H , the depth usually remains in the near-surface layer while for calculation of $Q_{H,20}$ the depth usually goes up to the subsurface layers of the ocean. Hence, the calculation of $Q_{H,20}$ includes the heat energies in the near surface and subsurface layers of the ocean. As such, if subsurface warming exceeds near-surface cooling, this may be seen as an increase in $Q_{H,20}$ post TC passage. Similarly, during

TC Winston, float R5904114 (located in the central region and moved a distance of 13 km post-TC passage) showed an increase in $Q_{H,20}$ of 13.8 kJ cm^{-2} post TC passage. The values of ΔH_A and ΔH_B estimated from float R5904114 were -23.7 and 46.6 kJ cm^{-2} respectively, which indicates subsurface warming exceeding near-surface cooling. However, due to the unavailability of in situ horizontal velocity profiles, a complete heat budget was not possible to confirm whether horizontal processes associated with ocean currents or eddies could account for this near-surface cooling and subsurface warming. As a result, while we do observe subsurface warming, we cannot confirm whether this is due to the TC. There is about a 10 day interval between each profile measurement from Argo floats. In the meantime, ocean currents and eddies may also produce these changes. However, examination of eddies and currents was beyond the scope of this study.

Perhaps future studies in this region could augment in situ observations with model or reanalysis ocean products to do a heat budget analysis to confirm which energy processes dominate. An interesting question to investigate in later studies could be to look more closely at whether this subsurface warming post-TC passage could be explained by vertical advection or if ocean currents and eddies play a greater role. Moreover, the Q_H and $Q_{H,20}$ profiles during TC Winston showed high variability and no consistent decrease post TC passage, unlike what was observed during TC Pam. Eddies could be playing a role and exploring TC-eddy interactions would be an interesting suggestion for future studies in the region. Float D503776 during TC Winston also showed an increase in both Q_H and $Q_{H,20}$ post-TC passage. This float was, however, not further analyzed as near this float, TC Winston was still in the tropical storm stage.

Both TCs were seen to intensify after passing over regions with high Q_H ($>60 \text{ kJ cm}^{-2}$). This is in agreement with previous studies using Q_H in intensity forecasts (e.g., Elsberry et al. 1976; Shay et al. 2000; Goni et al. 2009; Nagamani et al. 2012). Intensification was also seen in regions where heat fluxes were enhanced. The energy extracted by a TC is an order of magnitude less than Q_H (Cione and Uhlhorn 2003), however, over warm regimes where SST cooling is negligible, the energy extracted can be comparable to the changes in Q_H (Jaimes and Shay 2015). TC Winston, for instance, was rapidly weakening

as it moved northeast, away from Fiji. However, it passed over a region with high Q_H (calculated from float R5903568 to be 72.7 kJ cm^{-2}) just prior to recurving and began to intensify. Once TC Winston recurved, it again passed over a region with high Q_H (78.6 kJ cm^{-2}) and continued to intensify while it moved toward Fiji. Similarly, TC Pam had high Q_H available during the early stages of its lifetime, enabling it to intensify while it moved toward Vanuatu. The high Q_H available to TC Pam enabled it to retain category-5 strength for at least 2 days as it moved southward to higher latitudes.

Enhanced heat fluxes were observed about three days prior to TC Winston making landfall, with another short burst of enhanced heat fluxes in the core region of TC Winston just prior to its landfall (see Fig. S4). This short burst of enhanced heat fluxes could explain how TC Winston attained maximum intensity prior to making landfall. Previous studies on TC intensification such as Huang et al. (2017), who found large air-sea enthalpy heat fluxes contributing to the rapid intensification of Hurricane Patricia (2015), which occurred in the eastern Pacific region, is consistent with our finding of TC rapid intensification over regions of enhanced heat fluxes. Jaimes et al. (2015) analyzed bulk air-sea fluxes of enthalpy and momentum flux data acquired using dropsondes from 27 aircraft flights, in situ, and satellite observations for TC Earl (category-4 hurricane) and reported that intense local buoyant forcing was responsible for the intensification of TC Earl.

6. Summary and conclusions

The variability in SST and Q_H and $Q_{H,20}$ were explored along the tracks of two destructive TCs, TC Pam and TC Winston in the southwest Pacific region, that occurred during the years 2015 (March) and 2016 (February), respectively. The SST reductions post TC passage along the tracks of the TCs were as much as 5.4°C . SST reductions mostly within a range of $1^\circ\text{--}5^\circ\text{C}$ were observed for both the forced and relaxation stages of TC passage. Both Q_H and $Q_{H,20}$ decreased following the passage of both the TCs but more systematically in the case of TC Pam as compared to TC Winston. TC Winston showed large variability in both Q_H and $Q_{H,20}$ unlike TC Pam. This research has highlighted the use of $Q_{H,20}$ as a parameter that could be used to quantify the variability in ocean energy underneath a TC. Both these quantities are well correlated with r values varying between 0.47 and 0.95 for TC Pam and comparatively weak correlation for TC Winston (r values varying from 0.15 to 0.75).

The change in $Q_{H,20}$ post TC passage was used to identify the subsurface energy changes and effects of the TCs on the ocean. However, more work needs to be done to better understand the relationship between TC intensity and $Q_{H,20}$, as well as the impact of ocean currents and eddies on TCs in the region. OHC and heat fluxes are shown here to be important factors contributing to TC intensification. However, the intensity change of a TC is a complex, nonlinear process involving several competing or synergistic factors (Cione and Uhlhorn 2003) including an increase in thunderstorm activity prior to approximately 12–24 h of peak TC winds (Price et al. 2009; Zhang et al. 2015).

Future work could look at more TCs and incorporate additional atmospheric and oceanic parameters such as wind shear

and velocity profiles to complement the oceanic energy component, which are important for routine forecasting of TC intensity. High or low OHC may also be due to ocean currents or eddies. The interaction of TCs with ocean currents and cold-/warm-core eddies could be explored in future research for the southwest Pacific region.

Acknowledgments. The authors are thankful to financial support by The University of the South Pacific (USP), Fiji, under its Strategic Research Theme (Grant F7304-RI001-ACC-001) under which this work has been carried out. The authors would also like to acknowledge Dr Awnesh Singh at the Pacific Centre for Environment and Sustainable Development, USP, for his useful insight and comments on early parts of the work. The authors would also like to thank two anonymous reviewers for their comments, which greatly improved the manuscript. This research work relies on data sources: 1) TC best track data from the Southwest Pacific Enhanced Archive for Tropical Cyclones (SPEARTC; <http://apdrc.soest.hawaii.edu/projects/speartc/>). 2) High resolution SST data provided by JPL MUR MEASUREs Project (2015) GHRSSST Level 4 MUR Global Foundation Sea Surface Temperature Analysis (v4.1), version 4.1. PO.DAAC, California. Dataset at <https://doi.org/10.5067/GHGMR-4FJ04>; <https://podaac.jpl.nasa.gov/dataset/MUR-JPL-L4-GLOB-v4.1>. 3) Argo data: These data were collected and made freely available by the International Argo Program and the national programs that contribute to it. (<https://argo.ucsd.edu>, <https://www.ocean-ops.org>). The Argo Program is part of the Global Ocean Observing System. Argo (2000). Argo float data and metadata from Global Data Assembly Centre (Argo GDAC). SEANOE (<https://doi.org/10.17882/42182>). 4) Latent and sensible heat flux data were obtained from NOAA Climate Data Record of Ocean Heat Fluxes, version 2, <https://www.ncdc.noaa.gov/cdr/atmospheric/ocean-heat-fluxes>. These data sources are sincerely acknowledged.

REFERENCES

- Balaguru, K., P. Chang, R. Saravanan, L. R. Leung, Z. Xu, M. Li, and J.-S. Hsieh, 2012: Ocean barrier layers' effect on tropical cyclone intensification. *Proc. Natl. Acad. Sci. USA*, **109**, 14 343–14 347, <https://doi.org/10.1073/pnas.1201364109>.
- Bracken, W. E., and L. F. Bosart, 2000: The role of synoptic-scale flow during tropical cyclogenesis over the North Atlantic Ocean. *Mon. Wea. Rev.*, **128**, 353–376, [https://doi.org/10.1175/1520-0493\(2000\)128<0353:TROSSF>2.0.CO;2](https://doi.org/10.1175/1520-0493(2000)128<0353:TROSSF>2.0.CO;2).
- Chand, S. S., and K. J. E. Walsh, 2009: Tropical cyclone activity in the Fiji region: Spatial patterns and relationship to large-scale circulation. *J. Climate*, **22**, 3877–3893, <https://doi.org/10.1175/2009JCLI2880.1>.
- , and —, 2010: The influence of the Madden–Julian Oscillation on tropical cyclone activity in the Fiji region. *J. Climate*, **23**, 868–886, <https://doi.org/10.1175/2009JCLI3316.1>.
- , and —, 2011: Influence of ENSO on tropical cyclone intensity in the Fiji region. *J. Climate*, **24**, 4096–4108, <https://doi.org/10.1175/2011JCLI4178.1>.
- Chin, T. M., J. Vazquez-Cuervo, and E. M. Armstrong, 2017: A multi-scale high-resolution analysis of global sea surface temperature. *Remote Sen. Environ.*, **200**, 154–169, <https://doi.org/10.1016/j.rse.2017.07.029>.

- Cione, J. J., and E. W. Uhlhorn, 2003: Sea surface temperature variability in hurricanes: Implications with respect to intensity change. *Mon. Wea. Rev.*, **131**, 1783–1796, <https://doi.org/10.1175/2562.1>.
- Clayson, C. A., B. Jeremiah, and NOAA CDR Program, 2016: NOAA Climate Data Record Ocean Surface Bundle (OSB) Climate Data Record (CDR) of ocean heat fluxes, version 2. NOAA National Center for Environmental Information, accessed 8 March 2018, <https://doi.org/10.7289/V59K4885>.
- Dare, R. A., and J. L. McBride, 2011a: The threshold sea surface temperature condition for tropical cyclogenesis. *J. Climate*, **24**, 4570–4576, <https://doi.org/10.1175/JCLI-D-10-05006.1>.
- , and —, 2011b: Sea surface temperature response to tropical cyclones. *Mon. Wea. Rev.*, **139**, 3798–3808, <https://doi.org/10.1175/MWR-D-10-05019.1>.
- Elsberry, R. L., T. S. Fraim, and R. N. Trapnell, 1976: A mixed layer model of the oceanic thermal response to hurricanes. *J. Geophys. Res.*, **81**, 1153–1162, <https://doi.org/10.1029/JC081i006p01153>.
- Emanuel, K. A., 1986: An air-sea interaction theory for tropical cyclones. Part I: Steady-state maintenance. *J. Atmos. Sci.*, **43**, 585–605, [https://doi.org/10.1175/1520-0469\(1986\)043<0585: AASITF>2.0.CO;2](https://doi.org/10.1175/1520-0469(1986)043<0585: AASITF>2.0.CO;2).
- , 1999: Thermodynamic control of hurricane intensity. *Nature*, **401**, 665–669, <https://doi.org/10.1038/44326>.
- , 2001: Contribution of tropical cyclones to meridional heat transport by the oceans. *J. Geophys. Res.*, **106**, 14 771–14 781, <https://doi.org/10.1029/2000JD900641>.
- , 2005: Increasing destructiveness of tropical cyclones over the past 30 years. *Nature*, **436**, 686–688, <https://doi.org/10.1038/nature03906>.
- Fyfe, J., 2006: Southern Ocean warming due to human influence. *Geophys. Res. Lett.*, **33**, L19701, <https://doi.org/10.1029/2006GL027247>.
- Gill, A., 1984: On the behavior of internal waves in the wakes of storms. *J. Phys. Oceanogr.*, **14**, 1129–1151, [https://doi.org/10.1175/1520-0485\(1984\)014<1129:OTBOIW>2.0.CO;2](https://doi.org/10.1175/1520-0485(1984)014<1129:OTBOIW>2.0.CO;2).
- Goni, G., and Coauthors, 2009: Applications of satellite-derived ocean measurements to tropical cyclone intensity forecasting. *Oceanogr.*, **22**, 190–197, <https://doi.org/10.5670/oceanog.2009.78>.
- Gray, W. M., 1968: Global view of the origin of tropical disturbances and storms. *Mon. Wea. Rev.*, **96**, 669–700, [https://doi.org/10.1175/1520-0493\(1968\)096<0669:GVOTOO>2.0.CO;2](https://doi.org/10.1175/1520-0493(1968)096<0669:GVOTOO>2.0.CO;2).
- , 1988: Environmental influences on tropical cyclones. *Aust. Meteor. Mag.*, **36**, 127–139.
- Guan, S., W. Zhao, J. Huthnance, J. Tian, and J. Wang, 2014: Observed upper ocean response to Typhoon Megi (2010) in the northern South China Sea. *J. Geophys. Res. Oceans*, **119**, 3134–3157, <https://doi.org/10.1002/2013JC009661>.
- Gutro, R., 2015: Pam (Southern Pacific Ocean). Accessed 29 January 2017, <https://www.nasa.gov/content/goddard/pam-southern-pacific-ocean/>.
- , 2017: NASA sees Winston winding down near Norfolk Island. Accessed 29 January 2017, <https://www.nasa.gov/feature/goddard/2016/winston-southwestern-pacific-ocean>.
- Hart, R. E., R. N. Maue, and M. C. Watson, 2007: Estimating local memory of tropical cyclones through MPI anomaly evolution. *Mon. Wea. Rev.*, **135**, 3990–4005, <https://doi.org/10.1175/2007MWR2038.1>.
- Huang, H. C., J. Boucharel, I. I. Lin, F. F. Jin, C. C. Lien, and I. F. Pun, 2017: Air-sea fluxes for Hurricane Patricia (2015): Comparison with Supertyphoon Haiyan (2013) and under different ENSO conditions. *J. Geophys. Res. Oceans*, **122**, 6076–6089, <https://doi.org/10.1002/2017JC012741>.
- Jaimes, B., and L. K. Shay, 2009: Mixed layer cooling in mesoscale oceanic eddies during Hurricanes Katrina and Rita. *Mon. Wea. Rev.*, **137**, 4188–4207, <https://doi.org/10.1175/2009MWR2849.1>.
- , and —, 2015: Enhanced wind-driven downwelling flow in warm oceanic eddy features during the intensification of Tropical Cyclone Isaac (2012): Observations and theory. *J. Phys. Oceanogr.*, **45**, 1667–1689, <https://doi.org/10.1175/JPO-D-14-0176.1>.
- , —, and G. R. Halliwell, 2011: The response of quasigeostrophic oceanic vortices to tropical cyclone forcing. *J. Phys. Oceanogr.*, **41**, 1965–1985, <https://doi.org/10.1175/JPO-D-11-06.1>.
- , —, and E. W. Uhlhorn, 2015: Enthalpy and momentum fluxes during Hurricane Earl relative to underlying ocean features. *Mon. Wea. Rev.*, **143**, 111–131, <https://doi.org/10.1175/MWR-D-13-00277.1>.
- Jansen, M. F., R. Ferrari, and T. A. Mooring, 2010: Seasonal versus permanent thermocline warming by tropical cyclones. *Geophys. Res. Lett.*, **37**, L03602, <https://doi.org/10.1029/2009GL041808>.
- Jullien, S., and Coauthors, 2012: Impact of tropical cyclones on the heat budget of the South Pacific Ocean. *J. Phys. Oceanogr.*, **42**, 1882–1906, <https://doi.org/10.1175/JPO-D-11-0133.1>.
- , P. Marchesiello, C. E. Menkes, J. Lefevre, N. C. Jourdain, G. Samson, and M. Lengaigne, 2014: Ocean feedback to tropical cyclones: Climatology and processes. *Climate Dyn.*, **43**, 2831–2854, <https://doi.org/10.1007/s00382-014-2096-6>.
- Knaff, J. A., M. DeMaria, C. R. Sampson, J. E. Peak, J. Cummings, and W. H. Schubert, 2013: Upper oceanic energy response to tropical cyclone passage. *J. Climate*, **26**, 2631–2650, <https://doi.org/10.1175/JCLI-D-12-00038.1>.
- Knapp, K. R., M. C. Kruk, D. H. Levinson, H. J. Diamond, and C. J. Neumann, 2010: The International Best Track Archive for Climate Stewardship (IBTrACS). *Bull. Amer. Meteor. Soc.*, **91**, 363–376, <https://doi.org/10.1175/2009BAMS2755.1>.
- Korty, R. L., K. A. Emanuel, and J. R. Scott, 2008: Tropical cyclone-induced upper-ocean mixing and climate: Application to equable climates. *J. Climate*, **21**, 638–654, <https://doi.org/10.1175/2007JCLI1659.1>.
- Leipper, D. F., and D. Volgenau, 1972: Hurricane heat potential of the Gulf of Mexico. *J. Phys. Oceanogr.*, **2**, 218–224, [https://doi.org/10.1175/1520-0485\(1972\)002<0218:HHPOTG>2.0.CO;2](https://doi.org/10.1175/1520-0485(1972)002<0218:HHPOTG>2.0.CO;2).
- Lin, I. I., G. J. Goni, J. A. Knaff, C. Forbes, and M. M. Ali, 2013: Ocean heat content for tropical cyclone intensity forecasting and its impact on storm surge. *Nat. Hazards*, **66**, 1481–1500, <https://doi.org/10.1007/s11069-012-0214-5>.
- Ma, Z. H., J. F. Fei, X. G. Huang, and X. P. Cheng, 2013: The effects of ocean feedback on tropical cyclone energetics under idealized air-sea interaction conditions. *J. Geophys. Res. Atmos.*, **118**, 9778–9788, <https://doi.org/10.1002/JGRD.50780>.
- , —, L. Liu, X. G. Huang, and Y. Li, 2017: An investigation of the influences of mesoscale ocean eddies on tropical cyclone intensities. *Mon. Wea. Rev.*, **145**, 1181–1201, <https://doi.org/10.1175/MWR-D-16-0253.1>.
- McCaskill, C., L. K. Shay, J. K. Brewster, and P. C. Meyers, 2016: Development and assessment of the Systematically Merged Pacific Ocean Regional Temperature and Salinity (SPORTS) climatology for ocean heat content estimations. *J. Atmos. Oceanic Technol.*, **33**, 2259–2272, <https://doi.org/10.1175/JTECH-D-15-0168.1>.
- Mei, W., and C. Pasquero, 2013: Spatial and temporal characterization of sea surface temperature response to tropical cyclones. *J. Climate*, **26**, 3745–3765, <https://doi.org/10.1175/JCLI-D-12-00125.1>.
- Meyers, P., L. Shay, and J. Brewster, 2014: Development and analysis of the systematically merged Atlantic regional

- temperature and salinity climatology for oceanic heat content estimates. *J. Atmos. Oceanic Technol.*, **31**, 131–149, <https://doi.org/10.1175/JTECH-D-13-00100.1>.
- Meysignac, B., and Coauthors, 2019: Measuring global ocean heat content to estimate the Earth energy imbalance. *Front. Mar. Sci.*, **6**, 432, <http://doi.org/10.3389/fmars.2019.00432>.
- Nagamani, P. V., and Coauthors, 2012: Validation of satellite-derived tropical cyclone heat potential with in situ observations in the North Indian Ocean. *Remote Sens. Lett.*, **3**, 615–620, <https://doi.org/10.1080/01431161.2011.640959>.
- Park, J. J., Y. O. Kwon, and J. F. Price, 2011: Argo array observation of ocean heat content changes induced by tropical cyclones in the North Pacific. *J. Geophys. Res.*, **116**, C12025, <https://doi.org/10.1029/2011JC007165>.
- Pierce, D. W., T. P. Barnett, K. M. AchutaRao, P. J. Gleckler, J. M. Gregory, and W. M. Washington, 2006: Anthropogenic warming of the oceans: Observations and model results. *J. Climate*, **19**, 1873–1900, <https://doi.org/10.1175/JCLI3723.1>.
- Prasad, S., T. Aung, and A. Singh, 2009: Analysis of water properties and geostrophic currents in Fiji waters before and after Tropical Cyclone Gene. *Amer. J. Environ. Sci.*, **5**, 455–460, <https://doi.org/10.3844/AJESSP.2009.455.459>.
- Price, C., M. Asfur, and Y. Yair, 2009: Maximum hurricane intensity preceded by increase in lightning frequency. *Nat. Geosci.*, **2**, 329–332, <http://doi.org/10.1038/ngeo477>.
- Price, J. F., 1981: Upper ocean response to a hurricane. *J. Phys. Oceanogr.*, **11**, 153–175, [https://doi.org/10.1175/1520-0485\(1981\)011<0153:UORTAH>2.0.CO;2](https://doi.org/10.1175/1520-0485(1981)011<0153:UORTAH>2.0.CO;2).
- , 1983: Internal wave wake of a moving storm. Part I: Scales, energy budget, and observations. *J. Phys. Oceanogr.*, **13**, 949–965, [https://doi.org/10.1175/1520-0485\(1983\)013<0949:IWWOAM>2.0.CO;2](https://doi.org/10.1175/1520-0485(1983)013<0949:IWWOAM>2.0.CO;2).
- , R. A. Weller, and R. R. Schudlich, 1987: Wind-driven ocean currents and Ekman transport. *Science*, **238**, 1534–1538, <https://doi.org/10.1126/science.238.4833.1534>.
- , T. B. Sanford, and G. Z. Forristall, 1994: Forced stage response to a moving hurricane. *J. Phys. Oceanogr.*, **24**, 233–260, [https://doi.org/10.1175/1520-0485\(1994\)024<0233:FSRTAM>2.0.CO;2](https://doi.org/10.1175/1520-0485(1994)024<0233:FSRTAM>2.0.CO;2).
- Pun, I.-F., I.-I. Lin, and M.-H. Lo, 2013: Recent increase in high tropical cyclone heat potential area in the western North Pacific Ocean. *Geophys. Res. Lett.*, **40**, 4680–4684, <https://doi.org/10.1002/grl.50548>.
- Rayson, M. D., G. N. Ivey, N. L. Jones, R. J. Lowe, G. W. Wake, and J. D. McConchie, 2015: Near-inertial ocean response to tropical cyclone forcing on the Australian north-west shelf. *J. Geophys. Res. Oceans*, **120**, 7722–7751, <https://doi.org/10.1002/2015JC010868>.
- Riehl, H., 1950: A model of hurricane formation. *J. Appl. Phys.*, **21**, 917–925, <https://doi.org/10.1063/1.1699784>.
- Rudzin, J. E., L. K. Shay, and B. Jaimes de la Cruz, 2019: The impact of the Amazon–Orinoco River plume on enthalpy flux and air–sea interaction within Caribbean Sea tropical cyclones. *Mon. Wea. Rev.*, **147**, 931–950, <https://doi.org/10.1175/MWR-D-18-0295.1>.
- Sanford, T. B., J. F. Price, and J. B. Girton, 2011: Upper-ocean response to Hurricane Frances (2004) observed by profiling EM-APEX floats. *J. Phys. Oceanogr.*, **41**, 1041–1056, <https://doi.org/10.1175/2010JPO4313.1>.
- Sharma, K. K., D. C. Verdon-Kidd, and A. D. Magee, 2020: Decadal variability of tropical cyclogenesis and decay in the southwest Pacific. *Int. J. Climatol.*, **40**, 2811–2829, <https://doi.org/10.1002/joc.6368>.
- Shay, L. K., R. L. Elsberry, and P. G. Black, 1989: Vertical structure of the ocean current response to a hurricane. *J. Phys. Oceanogr.*, **19**, 649–669, [https://doi.org/10.1175/1520-0485\(1989\)019<0649:VSOTOC>2.0.CO;2](https://doi.org/10.1175/1520-0485(1989)019<0649:VSOTOC>2.0.CO;2).
- , G. J. Goni, and P. G. Black, 2000: Effects of a warm oceanic feature on Hurricane Opal. *Mon. Wea. Rev.*, **128**, 1366–1383, [https://doi.org/10.1175/1520-0493\(2000\)128<1366:EOAWOF>2.0.CO;2](https://doi.org/10.1175/1520-0493(2000)128<1366:EOAWOF>2.0.CO;2).
- Stowasser, M., Y. Wang, and K. Hamilton, 2007: Tropical cyclone changes in the western North Pacific in a global warming scenario. *J. Climate*, **20**, 2378–2396, <https://doi.org/10.1175/JCLI4126.1>.
- Swart, N. C., S. T. Gille, J. C. Fyfe, and N. P. Gillett, 2018: Recent Southern Ocean warming and freshening driven by greenhouse gas emissions and ozone depletion. *Nat. Geosci.*, **11**, 836–841, <https://doi.org/10.1038/s41561-018-0226-1>.
- Toffoli, A., J. McConchie, M. Ghantous, L. Loffredo, and A. Babanin, 2012: The effect of wave-induced turbulence on the ocean mixed layer during tropical cyclones: Field observations on the Australian north-west shelf. *J. Geophys. Res.*, **117**, C00J24, <https://doi.org/10.1029/2011JC007780>.
- von Schuckmann, K., and Coauthors, 2020: Heat stored in the Earth system: Where does the energy go? *Earth Syst. Sci. Data*, **12**, 2013–2041, <https://doi.org/10.5194/essd-12-2013-2020>.
- Wang, J.-W., and W. Han, 2014: The Bay of Bengal upper-ocean response to tropical cyclone forcing during 1999. *J. Geophys. Res. Oceans*, **119**, 98–120, <https://doi.org/10.1002/2013JC008965>.
- Wang, X. D., G. J. Han, Y. Q. Qi, and W. Li, 2011: Impact of barrier layer on typhoon-induced sea surface cooling. *Dyn. Atmos. Oceans*, **52**, 367–385, <https://doi.org/10.1016/j.dynatmoce.2011.05.002>.
- Yan, Y. F., L. Li, and C. Z. Wang, 2017: The effects of oceanic barrier layer on the upper ocean response to tropical cyclones. *J. Geophys. Res. Oceans*, **122**, 4829–4844, <https://doi.org/10.1002/2017JC012694>.
- Yulsman, T., 2016: How Winston become Earth’s strongest Southern Hemisphere storm in recorded history. Accessed 16 May 2017, <https://www.discovermagazine.com/environment/how-winston-became-earths-strongest-southern-hemisphere-storm-in-recorded-history>.
- Zedler, S. E., T. D. Dickey, S. C. Doney, J. F. Price, X. Yu, and G. L. Mellor, 2002: Analyses and simulations of the upper ocean’s response to Hurricane Felix at the Bermuda testbed mooring site: 13–23 August 1995. *J. Geophys. Res.*, **107**, 3232, <https://doi.org/10.1029/2001JC000969>.
- Zhai, X., R. J. Greatbatch, C. Eden, and T. Hibiya, 2009: On the loss of wind-induced near-inertial energy to turbulent mixing in the upper ocean. *J. Phys. Oceanogr.*, **39**, 3040–3045, <https://doi.org/10.1175/2009JPO4259.1>.
- Zhang, H., D. Chen, L. Zhou, X. Liu, T. Ding, and B. Zhou, 2016: Upper ocean response to Typhoon Kalmaegi (2014). *J. Geophys. Res. Oceans*, **121**, 6520–6535, <https://doi.org/10.1002/2016JC012064>.
- Zhang, J., Y. Lin, D. R. Chavas, and W. Mei, 2019: Tropical cyclone cold wake size and its applications to power dissipation and ocean heat uptake estimates. *Geophys. Res. Lett.*, **46**, 10177–10185, <https://doi.org/10.1029/2019GL083783>.
- Zhang, W., Y. Zhang, D. Zheng, F. Wang, and L. Xu, 2015: Relationship between lightning activity and tropical cyclone intensity over the northwest Pacific. *J. Geophys. Res. Atmos.*, **120**, 4072–4089, <https://doi.org/10.1002/2014JD022334>.